


## Crossed Andreev Reflection and Elastic Cotunneling in Three Quantum Dots Coupled by Superconductors

Alberto Bordin<sup>✉</sup>, Xiang Li, David van Driel<sup>✉</sup>, Jan Cornelis Wolff, Qingzhen Wang, Sebastiaan L. D. ten Haaf<sup>✉</sup>, Guanzhong Wang<sup>✉</sup>, Nick van Loosdrecht<sup>✉</sup>, Leo P. Kouwenhoven,<sup>\*</sup> and Tom Dvir<sup>✉†</sup>  
*QuTech and Kavli Institute of NanoScience, Delft University of Technology, 2600 GA Delft, The Netherlands*

 (Received 14 June 2023; revised 3 December 2023; accepted 5 January 2024; published 2 February 2024)

The formation of a topological superconducting phase in a quantum-dot–based Kitaev chain requires nearest neighbor crossed Andreev reflection and elastic cotunneling. Here, we report on a hybrid InSb nanowire in a three-site Kitaev chain geometry—the smallest system with well-defined bulk and edge—where two superconductor-semiconductor hybrids separate three quantum dots. We demonstrate pairwise crossed Andreev reflection and elastic cotunneling between both pairs of neighboring dots and show sequential tunneling processes involving all three quantum dots. These results are the next step toward the realization of topological superconductivity in long Kitaev chain devices with many coupled quantum dots.

DOI: [10.1103/PhysRevLett.132.056602](https://doi.org/10.1103/PhysRevLett.132.056602)

**Introduction.**—The Kitaev chain was proposed over two decades ago as a platform that supports unique nonlocal excitations known as Majorana bound states [1]. Proposals [2–4] for the realization of such a Kitaev chain rely on creating an array of spin-polarized quantum dots (QDs) where neighboring QDs are coupled via two mechanisms: elastic cotunneling (ECT) and crossed Andreev reflection (CAR). ECT involves the hopping of a single electron between two QDs. In CAR, two electrons from neighboring QDs simultaneously enter a superconductor to form a Cooper pair, or, in reversed order, two electrons forming a Cooper pair are split into two QDs [5–7]. Experiments have so far focused on chains consisting of two QDs, showing both CAR and ECT in such systems [8–21] and even strongly coupling the QDs to form a minimal Kitaev chain [22]. Longer QD chains, necessary for the formation of a topological phase, have so far not been realized.

In this Letter, we report on the fabrication of a three-site device and its characterization at zero magnetic field, where no isolated Majorana states are expected, but all the elements of a Kitaev chain Hamiltonian can already be tested. We show CAR and ECT between each pair of neighboring QDs and show that transport across the entire device is possible through sequential events of CAR and ECT. By measuring the currents on all of the terminals of our device, we identify all the possible CAR and ECT combinations.

**Device structure.**—In Fig. 1(a) we show a scanning electron micrograph of device A. This device consists of an InSb nanowire placed on top of an array of 11 finger gates separated by a thin dielectric. Two superconducting Al contacts (marked  $S_1$  and  $S_2$ ) are evaporated on top of the nanowire using the shadow-wall lithography technique [23,24]. Both sides of the device are further contacted

by two normal Cr/Au probes (marked  $N_L$  and  $N_R$ ). Every contact is connected to an independent voltage source ( $V_L$ ,  $V_{S1}$ ,  $V_{S2}$ ,  $V_R$ ) and current meter ( $I_L$ ,  $I_{S1}$ ,  $I_{S2}$ ,  $I_R$ ). The two finger gates underneath the semiconductor-superconductor hybrid segments control their chemical potential, while the other nine gates form QDs on each of the three bare InSb sections. The QD chemical potentials  $\mu_1$ ,  $\mu_2$ , and  $\mu_3$ , are controlled by the gate voltages  $V_{QD1}$ ,  $V_{QD2}$ , and  $V_{QD3}$ , respectively [Fig. 1(b)]. See Supplemental Material [25] for further nanofabrication details and gate settings.

**Results.**—Device characterization: Discrete Andreev bound states (ABSs) in a hybrid semiconductor-superconductor segment, separating two QDs, can efficiently mediate CAR and ECT between them [35–37]. We find such discrete states by controlling the two finger gates underneath contacts  $S_1$  and  $S_2$ . Figures 1(c) and 1(d) show the spectra measured on the first and the second hybrid, respectively, by using the finger gates separating the superconducting and normal contacts as tunneling barriers [38]. In the absence of an external magnetic field, both hybrid segments show a hard superconducting gap. A closer inspection of the gate dependence (see Fig. S3) shows that ABSs are present at energies close to the energy gap. At 150 mT, the ABSs are more visible in the spectrum. The remainder of the experiment was conducted at zero magnetic field and at fixed values of the hybrid gates.

In Figs. 1(e) and 1(f), we characterize QDs 1-3, respectively. QD<sub>1</sub> is characterized by applying a voltage bias to  $N_L$  and measuring the corresponding current while keeping all other contacts grounded. For QD<sub>2</sub> the voltage bias is applied to  $S_1$  and for QD<sub>3</sub> to  $N_R$ . During the characterization of a given QD, the other QDs are kept off-resonance. The observed Coulomb diamond structure allows us to estimate the charging energy of all QDs to

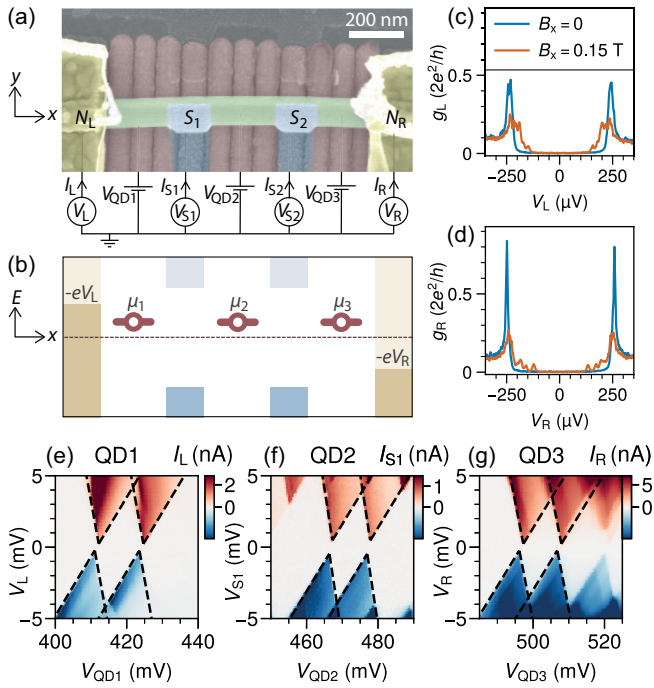


FIG. 1. (a) False-colored scanning electron micrograph of the device. An InSb nanowire (green) is deposited on top of 11 finger gates (red) and it is contacted with two superconducting leads  $S_1$  and  $S_2$  (blue) and two normal leads  $N_L$  and  $N_R$  (yellow). Every contact is connected to a corresponding voltage bias source and current meter. (b) Illustrative energy diagram. Brown symbols represent QD energy levels when occupied by an electron. (c),(d) Spectroscopy of the hybrid segments.  $g_L \equiv (dI_L/dV_L)$  and  $g_R \equiv (dI_R/dV_R)$  are obtained by numerical differentiation of the dc currents measured from the left and the right normal leads, respectively. Gate settings are reported in Supplemental Material (Figs. S2, S3, and S4). (e)–(g) Coulomb diamond characterization of QD<sub>1</sub> [panel (e)], QD<sub>2</sub> [panel (f)], QD<sub>3</sub> [panel (g)]. Fitting to a constant interaction model [34] yields charging energies of 4, 3.5, 3.3 mV and lever arms of 0.32, 0.33, 0.31 for QD<sub>1</sub>, QD<sub>2</sub>, and QD<sub>3</sub> respectively.

be between 3 and 4 mV and the lever arm of the underlying gates to be  $\approx 0.3$ . We note the presence of a superconducting gap in the spectrum.

**Pairwise CAR and ECT between neighboring QDs:**  
 We begin by demonstrating CAR and ECT processes between pairs of neighboring QDs. Figure 2(a) shows schematically how CAR between QD<sub>1</sub> and QD<sub>2</sub> is measured while QD<sub>3</sub> is kept off-resonance such that it does not participate in the transport. CAR involves current flowing from a superconductor into the neighboring leads (or vice versa). In recent works, CAR was measured setting symmetric voltage biases,  $V_b$ , on two normal leads on both sides of the hybrid segment [20,21,37]. Here, to account for the presence of the superconducting gap in  $S_2$  ( $\Delta \approx 230 \mu\text{eV}$ ), we apply a bias of  $V_b + \Delta/e$  to the superconducting leads. In this configuration, CAR can be sustained as long as  $\mu_1 = -\mu_2$  and the two chemical

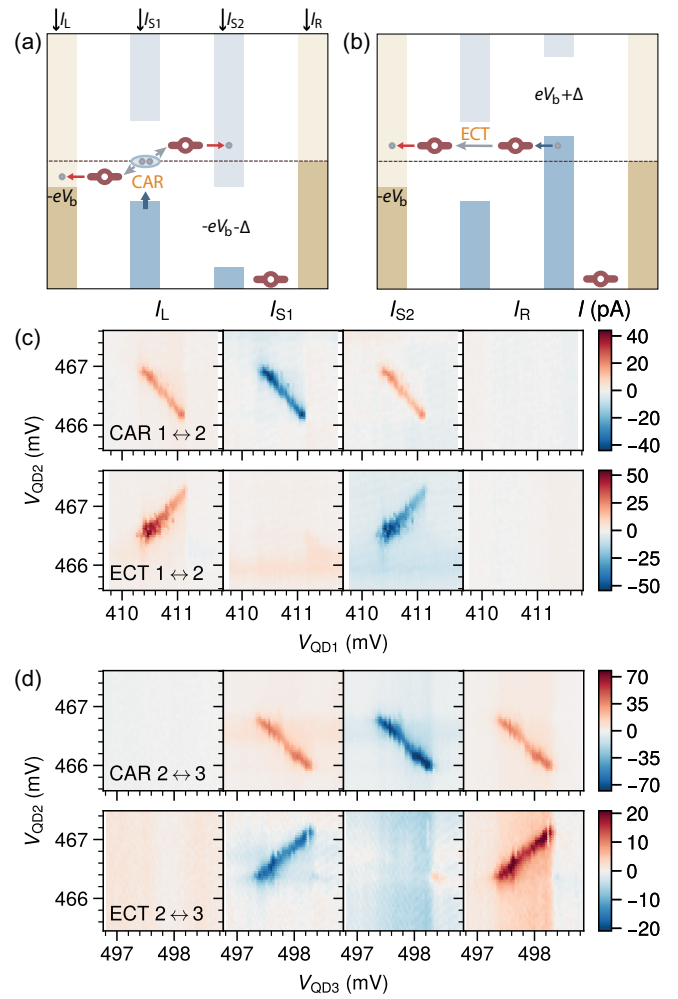


FIG. 2. (a),(b) Schematic diagrams of CAR and ECT processes between QD<sub>1</sub> and QD<sub>2</sub>. CAR is measured by applying  $V_b$  on  $N_L$  and  $V_b + \Delta/e$  on  $S_2$  [panel (a)]. ECT is measured by applying  $V_b$  on  $N_L$  and  $-V_b - \Delta/e$  on  $S_2$  [panel (b)]. (c) CAR and ECT between QD<sub>1</sub> and QD<sub>2</sub>. The currents  $I_L$ ,  $I_{S1}$ ,  $I_{S2}$ , and  $I_R$  are measured as a function of  $V_{QD1}$  and  $V_{QD2}$ .  $V_L = V_b = 150 \mu\text{V}$ , while  $V_{S2} = V_b + \Delta/e = 380 \mu\text{V}$  (top row) or  $V_{S2} = -380 \mu\text{V}$  (bottom row). (d) CAR and ECT between QD<sub>2</sub> and QD<sub>3</sub>. The currents through the leads as a function of  $V_{QD2}$  and  $V_{QD3}$  are measured with  $V_{S1} = 380 \mu\text{V}$  in the top row and  $V_{S1} = -380 \mu\text{V}$  in the bottom row, while  $V_R = 150 \mu\text{V}$ .

potentials are in the bias window  $-|eV_b| < \mu_1, \mu_2 < |eV_b|$  [20]. ECT can be measured in an antisymmetric bias configuration. Because of the presence of the superconducting gap, such a configuration similarly requires adding  $\Delta$  to the bias on  $S_2$ , as shown schematically in Fig. 2(b).

Figure 2(c) shows the currents through all leads measured in the bias configuration that allows for CAR (top row) and ECT (bottom row) as a function of  $V_{QD1}$  and  $V_{QD2}$ . In the top row, we find that the currents  $I_L$ ,  $I_{S1}$ , and  $I_{S2}$  are largest along a diagonal line consistent with  $\mu_1 = -\mu_2$ . Moreover,  $I_L$  and  $I_{S2}$  are positive and nearly equal, draining to the ground only through  $S_1$ . These

observations signal the presence of CAR between  $QD_1$  and  $QD_2$ . The bottom row is measured in a bias configuration that supports ECT. The measurements show finite  $I_L$  and  $I_{S2}$  currents with maxima along a diagonal compatible with  $\mu_1 = \mu_2$ . In this case,  $I_L$  and  $I_{S2}$  have opposite signs, and almost no current flows through  $S_1$ , signaling the presence of ECT.

Analogously, we measure CAR (and ECT) signatures between  $QD_2$  and  $QD_3$  by applying effectively symmetric (and antisymmetric) biases  $V_{S1}$  and  $V_R$  [Fig. 2(d)]. We also notice finite currents  $< 10$  pA that depend only on the value of  $V_{QD3}$ . We interpret this as a sign of local Andreev reflection (LAR) not being completely suppressed by the charging energy of  $QD_3$  (see also Fig. S4).

The results shown in Fig. 2 demonstrate both CAR and ECT—the crucial ingredients of a Kitaev chain—between every pair of QDs. We exploited here the freedom to bias each superconductor independently. This freedom might not always be accessible, e.g., in a Kitaev chain design with the superconductors connected in a loop. In the following, we discuss the signatures of CAR and ECT when both superconducting leads are grounded.

**Two-terminal CAR and ECT processes:** We set  $V_{S1} = V_{S2} = 0$ , and begin by discussing CAR and ECT processes between  $QD_2$  and  $QD_3$  while keeping  $QD_1$  off-resonance. We observe three transport mechanisms involving only leads  $S_2$  and  $N_R$ .

The first transport mechanism, already mentioned above, is LAR, which gives rise to a signal that depends only on the chemical potential of  $QD_3$ .

The second transport mechanism takes place when  $\mu_2 = \mu_3 = eV_{S2} = 0$ , as depicted in Fig. 3(a). In this alignment, both CAR and ECT are allowed. A Cooper pair can be transmitted from  $S_2$  to  $N_R$  by sequential CAR and ECT processes. First, a Cooper pair is split from  $S_2$  to

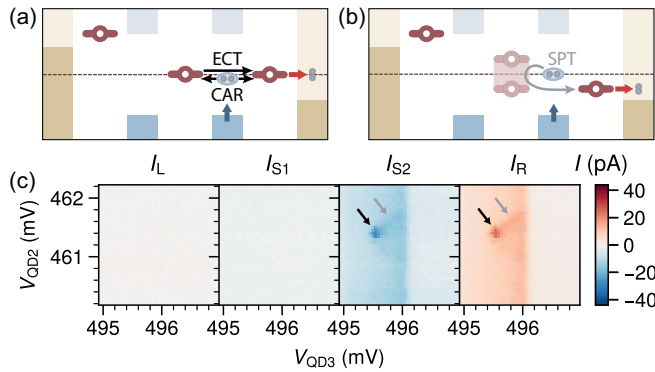


FIG. 3. (a) Schematic illustration of the resonant CAR and ECT tunneling. When  $\mu_2 = \mu_3 = 0$  both CAR and ECT are allowed between  $QD_2$  and  $QD_3$ , allowing a complete transport cycle to transfer a Cooper pair between  $N_R$  and  $S_2$ . (b) Schematic illustration of the Shiba-assisted local pair tunneling (SPT). (c) Current through the device as a function of  $V_{QD2}$  and  $V_{QD3}$ , with  $V_{QD1} = 414.1$  mV, equivalent to  $\mu_1 \approx 230$   $\mu$ eV.

$QD_2$  and  $QD_3$ . Then, the electron in  $QD_3$  is drained to  $N_R$ , allowing ECT to shuttle the other electron from  $QD_2$  to  $QD_3$ , which is finally drained as well. Because of the resonant condition on the chemical potentials, this process appears as a single spot in the measurements shown in Fig. 3(c) (black arrow).

When  $\mu_2 \neq 0$ , the resonant CAR-ECT process is not allowed anymore; however, a third transport mechanism can be observed. The gray arrow in Fig. 3(c) highlights a faint line showing local transport from  $S_2$  to  $N_R$  that is enhanced by  $QD_2$  alignment. We observe current flow when  $\mu_3$  is between 0 and  $-eV_R$  and the chemical potentials of  $QD_2$  and  $QD_3$  are either aligned or antialigned. Following literature, this process may be interpreted as “Shiba-assisted local pair tunneling” (SPT) [18,39], which is depicted schematically in Fig. 3(b). Further details of such process and additional data are discussed in Supplemental Material (Fig. S6).

**Three-dot sequential CAR and ECT:** When setting  $|\mu_1| < |eV_L|$ ,  $QD_1$  can participate in transport, enabling sequential CAR and ECT processes involving all three QDs. Figure 4(a) shows schematically such processes with antisymmetric bias settings ( $V_L = -V_R$ ). In this configuration, electrons incoming from  $N_L$  can be transferred all the way to  $N_R$ , in two ways. Sequential ECT events

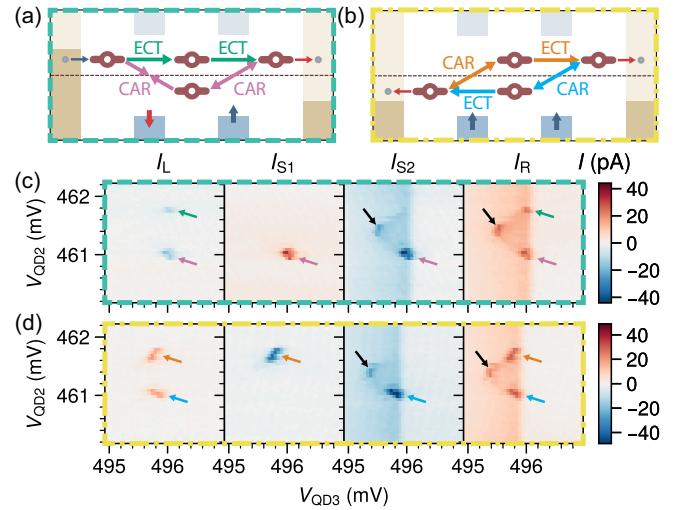


FIG. 4. (a) Schematic illustration of sequential ECT processes (with  $\mu_1 = \mu_2 = \mu_3$ , green) and sequential CAR processes (with  $\mu_1 = -\mu_2 = \mu_3$ , pink). (b) Schematic illustration of CAR followed by ECT (with  $-\mu_1 = \mu_2 = \mu_3$ , orange) and ECT followed by CAR (with  $\mu_1 = \mu_2 = -\mu_3$ , blue). (c) Current through the device as a function of  $V_{QD2}$  and  $V_{QD3}$ , with  $V_R = -V_L = 150$   $\mu$ V and  $V_{QD1} = 413.8$  mV, equivalent to  $\mu_1 \approx 130$   $\mu$ eV. (d) Current through the device as a function of  $V_{QD2}$  and  $V_{QD3}$ , with  $V_R = V_L = 150$   $\mu$ V and  $V_{QD1} = 413$  mV, equivalent to  $\mu_1 \approx -100$   $\mu$ eV. Note that the arrow colors in panels (c) and (d) correspond to the process colors in panels (a) and (b), while the black arrow corresponds to the resonant CAR and ECT process shown in Figs. 3(a) and 3(c).

(green arrows) can first transfer an electron from  $QD_1$  to  $QD_2$  and then from  $QD_2$  to  $QD_3$ , provided that the QD chemical potentials are all aligned ( $\mu_1 = \mu_2 = \mu_3$ ). Alternatively, if the QD chemical potentials are antialigned ( $\mu_1 = -\mu_2 = \mu_3$ ), sequential CAR events can first form a Cooper pair into  $S_1$  and then split a Cooper pair from  $S_2$ , resulting in a net transfer of one electron from  $QD_1$  to  $QD_3$  (pink arrows). Equivalently, this sequential CAR process can be seen as an electron from  $QD_1$  being converted into a hole in  $QD_2$  and converted back to an electron into  $QD_3$ .

Figure 4(c) shows measured currents as a function of  $V_{QD2}$  and  $V_{QD3}$  for fixed  $V_R = -V_L$ . We observe both the two-QD processes discussed above (see black arrows) and the three-QD processes discussed here. Sequential ECT processes appear as a single spot in only  $I_L$  and  $I_R$ , when  $\mu_2$  and  $\mu_3$  are aligned with  $\mu_1$  (marked by the green arrow). The sequence involving two CAR processes (marked by the pink arrow) appears as a spot in the currents measured on all leads when  $\mu_3 = \mu_1$  and  $\mu_2 = -\mu_1$ . The currents alter in sign at every lead, corresponding to Cooper pair formation in  $S_1$  followed by Cooper pair splitting in  $S_2$ . We note that also the amount of measured current is consistent with CAR, showing in the superconducting leads twice the amount of current registered in the normal leads.

Under symmetric bias conditions, current is sustained when both leads  $N_L$  and  $N_R$  drain electrons [see Fig. 4(b)]. The two sequences involving all QDs in agreement with this condition are CAR followed by ECT and the opposite, ECT followed by CAR. The first, marked by the orange arrow in Fig. 4(d), is seen in the current appearing when  $\mu_3 \approx \mu_2 \approx -\mu_1$  in  $I_L$  and  $I_R$ . This feature further appears in  $I_{S1}$  but not in  $I_{S2}$ , since CAR between  $QD_1$  and  $QD_2$  drains current to the ground through  $S_1$ , whereas ECT between  $QD_2$  and  $QD_3$  drains no such current to ground via  $S_2$ . The opposite sequence, marked by the blue arrow, takes place with  $\mu_3 \approx -\mu_2 \approx -\mu_1$  and shows similar behavior. We emphasize that this coupling between all three sites gives rise to a nonlocal transport feature. For example, we observe in Figs. 4(c) and 4(d) that  $I_L$  is strongly modulated by  $QD_3$ , two sites away.

These observations are consistent with CAR and ECT in the energy alignment of the QDs, in the signs and in the amounts of the measured currents, for every voltage bias combination (see additional data in the linked repository). So far, we have shown CAR and ECT signatures from two different points of view: pairwise in Fig. 2 and sequential at fixed  $QD_1$  in Fig. 4. In Fig. 5, we add a third one, noticing that both sequential ECT processes and sequential CAR processes always require  $\mu_1 = \mu_3$ , whereas CAR followed by ECT and ECT followed by CAR require  $\mu_1 = -\mu_3$ . In Fig. 5, we measure the currents through the devices while tuning the QDs to follow these constraints. Figure 5(a) was measured by setting  $V_R = -V_L = 150 \mu\text{V}$ .  $V_{QD1}$  and  $V_{QD3}$  were swept together, imposing  $\mu_1 = \mu_3$  for the full

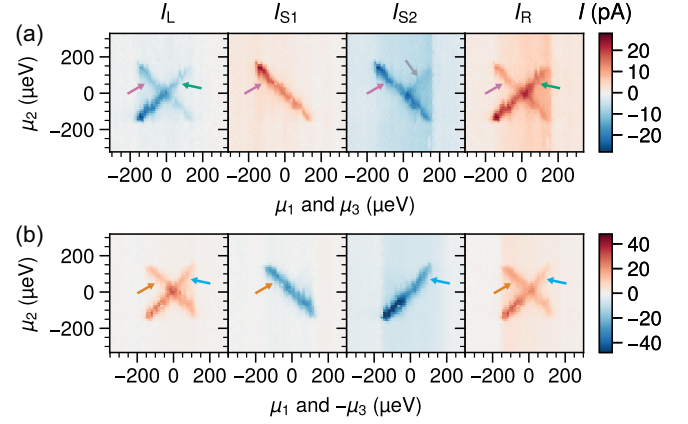


FIG. 5. (a) Current through the device as a function of  $\mu_2$  and jointly  $\mu_1$  and  $\mu_3$ , which are set to equal values, measured with antisymmetric bias configuration. (b) Current through the device as a function of  $\mu_2$  and jointly  $\mu_1$  and  $\mu_3$ , which are set to opposite values, measured with symmetric bias configuration. Note that the color of the arrows corresponds to the color of the processes in Fig. 4 (and 3 for the gray arrow).

measurement (see Fig. S5 in Supplemental Material 3wfor details regarding the tuning of chemical potential). Figure 5(a) features two diagonal lines. The positive-slope diagonal, compatible with  $\mu_1 = \mu_2 = \mu_3$ , is prominent in panels  $I_L$  and  $I_R$  only, allowing us to attribute it to sequential ECT processes. The negative-slope diagonal, compatible with  $\mu_1 = -\mu_2 = \mu_3$ , appears in all panels and is associated with sequential CAR processes. The measurements in Fig. 5(b) were conducted with  $V_R = V_L = 150 \mu\text{V}$ . Here,  $V_{QD1}$  and  $V_{QD3}$  are varied together, while imposing  $\mu_1 = -\mu_3$ . Similarly to the previous scenario, measured currents feature a positive-slope diagonal alongside a negative-slope one. Here, the positive-slope diagonal involves  $I_{S2}$  as expected for ECT followed by CAR. The negative-slope diagonal involves  $I_{S1}$  instead, as required by CAR followed by ECT.

In summary, the results of Figs. 4 and 5 show how all four possible compositions of CAR and ECT mediate transport through the entire device.

**Conclusion.**—We have fabricated and measured an InSb-Al device with three QDs separated by semiconductor-superconductor hybrids, showing the signatures of CAR and ECT between all pairs of neighboring QDs. We have further demonstrated control over sequential CAR and ECT processes involving all QDs by tuning the biases applied to the normal leads and the chemical potential of the QDs. Our measurements demonstrate the operation of all the known requirements to extend the Kitaev chain physics to longer multisite chains. To enable the formation of a three-site Kitaev chain in such devices, future work will focus on fine-tuning the interdot couplings at a finite magnetic field to balance the pairwise CAR and ECT ratios to observe the emergence of Majorana bound states at the chain ends.

Finally, we note that the scope of the experiments presented further demonstrates a general platform enabling long-range entanglement in condensed matter systems [5,40]. For instance, we note that three sequential CAR events involving four QDs realizes a simple entanglement swapping scheme [41,42].

All raw data in the publication and the analysis code used to generate figures are available at [43]. In the same repository, we share in addition a complete dataset of three-dimensional current measurements as a function of  $V_{\text{QD1}}$ ,  $V_{\text{QD2}}$ , and  $V_{\text{QD3}}$  for all combinations of symmetric and antisymmetric biases ( $V_{\text{b}} = \pm V_{\text{L}} = \pm V_{\text{R}}$ ). We share a similar dataset for a second device as well (see also Fig. S7 in Supplemental Material). We include GIF animations for better visualization.

This work has been supported by the Dutch Organization for Scientific Research (NWO) and Microsoft Corporation Station Q. We wish to acknowledge Srijit Goswami, Francesco Zatelli, and Greg Mazur for useful discussions and Ghada Badawy, Sasa Gazibegovic, and Erik P. A. M. Bakkers for the nanowire growth. A. B., X. L., J. C. W., and D. v.-D. fabricated the devices. A. B. and X. L. performed the electrical measurements with help from Q. W. and S. L. D. t.-H. A. B. and T. D. designed the experiment and analyzed the data. T. D. and L. P. K. supervised the project. A. B., T. D., and L. P. K. prepared the manuscript with input from all authors.

\*i.p.kouwenhoven@tudelft.nl

†tom.dvir@gmail.com

- [1] A. Y. Kitaev, *Phys. Usp.* **44**, 131 (2001).
- [2] J. D. Sau and S. D. Sarma, *Nat. Commun.* **3**, 964 (2012).
- [3] M. Leijnse and K. Flensberg, *Phys. Rev. B* **86**, 134528 (2012).
- [4] I. C. Fulga, A. Haim, A. R. Akhmerov, and Y. Oreg, *New J. Phys.* **15**, 045020 (2013).
- [5] P. Recher, E. V. Sukhorukov, and D. Loss, *Phys. Rev. B* **63**, 165314 (2001).
- [6] G. B. Lesovik, T. Martin, and G. Blatter, *Eur. Phys. J. B* **24**, 287 (2001).
- [7] O. Sauret, D. Feinberg, and T. Martin, *Phys. Rev. B* **70**, 245313 (2004).
- [8] L. Hofstetter, S. Csonka, J. Nygård, and C. Schönenberger, *Nature (London)* **461**, 960 (2009).
- [9] L. G. Herrmann, F. Portier, P. Roche, A. L. Yeyati, T. Kontos, and C. Strunk, *Phys. Rev. Lett.* **104**, 026801 (2010).
- [10] J. Wei and V. Chandrasekhar, *Nat. Phys.* **6**, 494 (2010).
- [11] L. Hofstetter, S. Csonka, A. Baumgartner, G. Fülöp, S. d'Hollosy, J. Nygård, and C. Schönenberger, *Phys. Rev. Lett.* **107**, 136801 (2011).
- [12] A. Das, Y. Ronen, M. Heiblum, D. Mahalu, A. V. Kretinin, and H. Shtrikman, *Nat. Commun.* **3**, 1165 (2012).
- [13] J. Schindele, A. Baumgartner, and C. Schönenberger, *Phys. Rev. Lett.* **109**, 157002 (2012).
- [14] J. Schindele, A. Baumgartner, R. Maurand, M. Weiss, and C. Schönenberger, *Phys. Rev. B* **89**, 045422 (2014).
- [15] Z. B. Tan, D. Cox, T. Nieminen, P. Lähteenmäki, D. Golubev, G. B. Lesovik, and P. J. Hakonen, *Phys. Rev. Lett.* **114**, 096602 (2015).
- [16] J. Gramich, A. Baumgartner, and C. Schönenberger, *Phys. Rev. B* **96**, 195418 (2017).
- [17] S. Baba, C. Jünger, S. Matsuo, A. Baumgartner, Y. Sato, H. Kamata, K. Li, S. Jeppesen, L. Samuelson, H. Xu *et al.*, *New J. Phys.* **20**, 063021 (2018).
- [18] Z. Scherübl, G. Fülöp, C. P. Moca, J. Gramich, A. Baumgartner, P. Makk, T. Elalaily, C. Schönenberger, J. Nygård, G. Zaránd *et al.*, *Nat. Commun.* **11**, 1834 (2020).
- [19] A. Ranni, F. Brange, E. T. Mannila, C. Flindt, and V. F. Maisi, *Nat. Commun.* **12**, 6358 (2021).
- [20] G. Wang, T. Dvir, G. P. Mazur, C.-X. Liu, N. van Loo, S. L. ten Haaf, A. Bordin, S. Gazibegovic, G. Badawy, E. P. Bakkers *et al.*, *Nature (London)* **612**, 448 (2022).
- [21] Q. Wang, S. L. ten Haaf, I. Kulesh, D. Xiao, C. Thomas, M. J. Manfra, and S. Goswami, *arXiv:2211.05763*.
- [22] T. Dvir, G. Wang, N. v. Loo, C.-X. Liu, G. P. Mazur, A. Bordin, S. L. D. t. Haaf, J.-Y. Wang, D. v. Driel, F. Zatelli, X. Li, F. K. Malinowski, S. Gazibegovic, G. Badawy, E. P. A. M. Bakkers, M. Wimmer, and L. P. Kouwenhoven, *Nature (London)* **614**, 445 (2023).
- [23] S. Heedt, M. Quintero-Pérez, F. Borsoi, A. Fursina, N. v. Loo, G. P. Mazur, M. P. Nowak, M. Ammerlaan, K. Li, S. Korneychuk, J. Shen, M. A. Y. v. d. Poll, G. Badawy, S. Gazibegovic, N. d. Jong, P. Aseev, K. v. Hoogdalem, E. P. A. M. Bakkers, and L. P. Kouwenhoven, *Nat. Commun.* **12**, 4914 (2021).
- [24] G. P. Mazur, N. v. Loo, J. Wang, T. Dvir, G. Wang, A. Khindanov, S. Korneychuk, F. Borsoi, R. C. Dekker, G. Badawy, P. Vinke, S. Gazibegovic, E. P. A. M. Bakkers, M. Q. Pérez, S. Heedt, and L. P. Kouwenhoven, *Adv. Mater.* **34**, 2202034 (2022).
- [25] See Supplemental Material at <http://link.aps.org/supplemental/10.1103/PhysRevLett.132.056602> for additional setup details, supporting measurements, and discussion of Shiba-assisted pair tunneling, which includes Refs. [26–33].
- [26] G. Badawy, S. Gazibegovic, F. Borsoi, S. Heedt, C.-A. Wang, S. Koelling, M. A. Verheijen, L. P. Kouwenhoven, and E. P. Bakkers, *Nano Lett.* **19**, 3575 (2019).
- [27] Michiel de Moor, Ph.D. thesis, Delft University of Technology, 2019.
- [28] Y. Luh, *Acta Phys. Sin.* **21**, 75 (1965).
- [29] H. Shiba, *Prog. Theor. Phys.* **40**, 435 (1968).
- [30] A. Rusinov, *JETP Lett.* **9** (1969), [http://jetpletters.ru/ps/1658/article\\_25295.shtml](http://jetpletters.ru/ps/1658/article_25295.shtml).
- [31] J. Bauer, A. Oguri, and A. C. Hewson, *J. Phys. Condens. Matter* **19**, 486211 (2007).
- [32] T. Meng, S. Florens, and P. Simon, *Phys. Rev. B* **79**, 224521 (2009).
- [33] E. J. H. Lee, X. Jiang, M. Houzet, R. Aguado, C. M. Lieber, and S. D. Franceschi, *Nat. Nanotechnol.* **9**, 79 (2014).
- [34] R. Hanson, L. M. K. Vandersypen, L. H. Willems van Beveren, J. M. Elzerman, I. T. Vink, and L. P. Kouwenhoven, *Phys. Rev. B* **70**, 241304(R) (2004).

- [35] G. Fülöp, F. Domínguez, S. d'Hollosy, A. Baumgartner, P. Makk, M. Madsen, V. Guzenko, J. Nygård, C. Schönenberger, A. L. Yeyati, and S. Csonka, *Phys. Rev. Lett.* **115**, 227003 (2015).
- [36] C.-X. Liu, G. Wang, T. Dvir, and M. Wimmer, *Phys. Rev. Lett.* **129**, 267701 (2022).
- [37] A. Bordin, G. Wang, C.-X. Liu, S. L. ten Haaf, G. P. Mazur, N. van Loo, D. Xu, D. van Driel, F. Zatelli, S. Gazibegovic *et al.*, *Phys. Rev. X* **13**, 031031 (2023).
- [38] D. van Driel, G. Wang, A. Bordin, N. van Loo, F. Zatelli, G. P. Mazur, D. Xu, S. Gazibegovic, G. Badawy, E. P. Bakkers *et al.*, *Nat. Commun.* **14**, 6880 (2023).
- [39] Z. Scherübl, G. Fülöp, J. Gramich, A. Pályi, C. Schönenberger, J. Nygård, and S. Csonka, *Phys. Rev. Res.* **4**, 023143 (2022).
- [40] M.-S. Choi, C. Bruder, and D. Loss, *Phys. Rev. B* **62**, 13569 (2000).
- [41] C. H. Bennett, G. Brassard, C. Crépeau, R. Jozsa, A. Peres, and W. K. Wootters, *Phys. Rev. Lett.* **70**, 1895 (1993).
- [42] M. Zukowski, A. Zeilinger, M. A. Horne, and A. K. Ekert, *Phys. Rev. Lett.* **71**, 4287 (1993).
- [43] A. Bordin and T. Dvir, version 1, name: Crossed Andreev reflection and elastic co-tunneling in a three-site Kitaev chain nanowire device (2023), [10.5281/zenodo.8021183](https://doi.org/10.5281/zenodo.8021183).